RSC Advances

This is an *Accepted Manuscript*, which has been through the Royal Society of Chemistry peer review process and has been accepted for publication.

Accepted Manuscripts are published online shortly after acceptance, before technical editing, formatting and proof reading. Using this free service, authors can make their results available to the community, in citable form, before we publish the edited article. This *Accepted Manuscript* will be replaced by the edited, formatted and paginated article as soon as this is available.

You can find more information about *Accepted Manuscripts* in the Information for Authors.

Please note that technical editing may introduce minor changes to the text and/or graphics, which may alter content. The journal's standard Terms & Conditions and the Ethical guidelines still apply. In no event shall the Royal Society of Chemistry be held responsible for any errors or omissions in this *Accepted Manuscript* or any consequences arising from the use of any information it contains.

ROYAL SOCIETY OF CHEMISTRY

www.rsc.org/advances

Journal Name

ARTICLE

Received 00th January 20xx,
Accepted 00th January 20xx

DOI: 10.1039/x0xx00000x

www.rsc.org/

Stability enhancement of organic photovoltaic devices utilizing partially reduced graphene oxide as the hole transport layer: nanoscale insight into structural/interfaces properties and aging effects

B. Paci,[a] G. Kakavelakis,[b] A. Generosi,[a] V. Rossi Albertini,[a] J. P. Wright,[c] C. Ferrero,[c] D. Konios,[b] E. Stratakis,[b,d] and E. Kymakis[b*]

A powerfull insight into the structural and interfacial properties of post-fabricated bulk heterojunction (BHJ) organic photovoltaic (OPV) devices is reported. The nanoscale local structure of integrated devices is revealed by combined X-ray diffraction (XRD) and fluorescence (XRF) investigations. A comparative study is performed on devices using graphene oxide (GO) as the hole transporting layer (HTL) and reference PEDOT:PSS (poly(3,4 ethylenedioxythiophene): poly(styrenesulfonate)) devices. Spatially resolved simultaneous XRD/XRF measurements with nanometre resolution on pristine and aged states of the devices evidence the occurrence of morphological modifications in the poly(2,7-carbazole) derivative (PCDTBT):fullerene derivative ($PC_{71}BM$) active layer, induced by thermal reduction and solar illumination. Additionally, the results indicate that OPV devices with partially reduced graphene oxide (pr-GO) used as HTL, exhibit photovoltaic characteristics similar to the PEDOT:PSS based devices but with a significant durability enhancement. This is attributed to the protecting role of the pr-GO film against humidity and Indium diffusion from the Indium Tin Oxide (ITO) anode into the photoactive layer. As a result, the devices fabricated with pr-GO-HTL retain approximately 65% of their initial power conversion efficiency over 20hours, while the efficiency of the reference devices degrades to 45% of the initial value.

1.Introduction

Over the last decade, BHJ organic photovoltaic devices have become an increasingly exciting area of research due to several potential advantages, including light weight, flexibility, low cost large-scale production and have been considered as the ideal alternative technology to silicon-based pn-junction solar cells.[1-3] Extensive research efforts have been made to improve the power conversion efficiency (PCE) and the stability of OPV devices, the rapid progress in materials design and device architectures being the main reasons for breaking the 10% barrier for PCE.[4-5]

In a typical BHJ OPV device, the photoactive layer composed of a conjugated polymer as the electron donor and a fullerene derivative as the electron acceptor is sandwiched between the transparent conductive anode (usually ITO) and the metal cathode (low work function metal). The introduction of interfacial layers with hole and electron transport properties, between the donor-acceptor active blend and the anode on the one hand and the anode and cathode on the other hand, enable the unipolar extraction of photogenerated carriers from the photoactive layer to the electrodes.[6] Titanium suboxide (TiO_x) is the current state-of-the-art electron transport layer (ETL) material, while PEDOT:PSS is the most regularly used HTL.[7,8] The advantages of using PEDOT:PSS include solution processability, sufficient conductivity and high optical transparency in the visible-NIR regime.[9] However, there are several drawbacks originating from the nature of PEDOT:PSS, which leads to reduced lifetime and OPV failure. Its highly acidic (pH∼1) aqueous suspension has been shown to corrode ITO and also diffuses water molecules into the active layer, eventually reducing device performances and long-term stability.[10,11]

Graphene, an atomically thin layer of sp2-bonded carbon atoms, stacked in a two-dimensional (2D) honeycomb lattice, has attracted great interest in the scientific community for its extraordinary electrical and optical properties, the mechanical flexibility, its tuneable work function (WF), which gives rise to its utilization for various components in several applications.[12-15] Recently, GO, a graphene derivative, has been used as an alternative to PEDOT:PSS HTL, owing to its high transparency,

a. Istituto di Struttura della Materia, CNR, Via del Fosso del Cavaliere 100, 00133 Roma, Italy.
b. Center of Materials Technology & Photonics Technological Educational Institute (TEI) of Crete and, Electrical Engineering Department TEI of Crete, Heraklion 71004 Crete, Greece. Email: kymakis@staff.teicrete.gr
c. European Synchrotron Radiation Facility 6, Jules Horowitz, 38000 Grenoble, France.
d. Institute of Electronic Structure and Laser (IESL), Foundation for Research and Technology Hellas (FORTH), & Dept. Of Materials Science and Technology, Univ. Of Crete, Heraklion, Crete, Greece.

RSC Advances Accepted Manuscript

its tuneable WF and its processability in solution.[16,17] Whilst the zero band gap of pristine graphene prohibits its application to charge blocking layers, GO (produced by oxidation of graphite) exhibits a tuneable band gap[18,19] and improved solubility in various solvents,[20] making it compatible with roll-to-roll mass production processes and triggering its use in printed flexible electronics.[21] Nevertheless, next generation graphene-based HTL materials[22] must overcome the corrosive and other undesirable properties of PEDOT:PSS, negatively affecting the long term device stability.

Doubtlessly, in the research of the driving mechanisms of OPV device degradation, the role of structural/morphological properties of the different layers composing these multi-layered systems and their interfaces is a key point to evaluate carefully.[23-26] Besides that, optical transport properties are roughly related to the structure, morphology and interfacial characteristics of the device components[27-32] as well as their stability.[33-37]

An important issue to be noted and which has not been raised in previous reports on GO-based HTLs, is that the deposited material on the ITO electrode is initially a GO-film, which is actually modified to a partially reduced GO during the subsequent fabrication steps of the device, causing removal of oxygen functional groups. In particular, in OPV devices based on P3HT (poly(3-hexylthiophene-2,5-diyl)) a post-fabrication annealing of the device takes places at ~160°C in order to achieve an acceptable PCE, a process that actually induces a partial reduction in the as deposited GO thin film.[16,38-40] Similarly, in the case of thermosensitive low bandgap polymers (PCDTBT etc.), in which a high temperature post-fabrication treatment negatively affects the device performance, partial reduction of the GO-film by either thermal[41,44] or photochemical[19,43-45] effect is necessary in order for the devices to exhibit a performance comparable or superior to PEDOT:PSS. In addition, a huge amount of studies have reported non-thermal, light-induced reduction of GO[46-48] indicating that a reduction process might take place during the OPV device illumination. From the above findings, it is more than clear that the as-prepared GO thin films performance is not comparable with PEDOT:PSS, and a partial reduction always takes place. On the other hand, research has been so far focused on the comparison between the performance of graphene-based HTLs and the one of PEDOT:PSS devices.[19,37] As a result, there is currently a lack of studies concerning the stability of OPV devices employing GO HTLs. Accordingly, there is room for extensive research efforts towards identifying the various device degradation mechanisms, and clarify their role in the overall efficiency deterioration.

In this context, this study aims to compare the effect of GO and pr-GO HTLs on the OPV device stability versus degradation. This is investigated by high spatial resolution synchrotron XRD experiments, performed in the pristine as well as under solar illuminated states. This powerful technique is applied to post-fabricated OPV devices and allows assessing structure-property relations that link length scales from local nano/hetero structures and interfaces with large scale devices. Owing to the high spatial resolution, the molecular ordering of the active layer polymer component of devices with GO-based HTL can be detected and compared to that of devices featuring PEDOT:PSS.

2.Experimental

2.1 Device fabrication and measurements

2.1.1 Preparation of Graphene Oxide. GO was prepared from graphite powder (Alfa Aesar ~200 mesh) according to a modified Hummers' method. In more detail,[49] graphite powder (1.0 g) was put into a mixture of H_2SO_4 (23 mL, 98%) and $NaNO_3$ (0.5 g). The mixture was then stirred and cooled in an ice bath. While maintaining vigorous stirring, $KMnO_4$ (3.0 g) was then added in portions over a period of 2 h. The reaction mixture was left for 4 h in order to reach room temperature before being heated to 35 °C for 30 min. It was then poured into a flask containing deionised water (50 mL) and further heated to 70 °C for 15 min. The mixture was then decanted into 250 mL of deionised water and the unreacted $KMnO_4$ was removed by adding 3% H_2O_2. The reaction mixture was then left for some time to settle and decant. The graphite oxide obtained was then purified by repeated centrifugation and redispersed in deionised water until a negative reaction on sulfate ion (with $Ba(NO_3)_2$) was achieved. Finally, the resulting GO was dried at 60 °C in a vacuum oven for 48 h before use.

2.1.2 Preparation of Titanium suboxide solution. TiO_x solution preparation:[50] Titanium (IV) isopropoxide ($Ti[OCH(CH_3)_2]_4$, 5 mL), 2-methoxyethanol ($CH_3OCH_2CH_2OH$, 20 mL) and ethanolamine ($H_2NCH_2CH_2OH$, 2 mL) were added to a three-necked flask in nitrogen atmosphere. The solution was then stirred for 1 h at room temperature, followed by heating first at 80 °C for 1 h and then at 120 °C for another 1 h. The solution was eventually cooled to room temperature and 10 mL of isopropanol were added.

2.1.3 Device fabrication and measurements. PCDTBT:$PC_{71}BM$ was dissolved in 1,2-dichlorobenzene:Chlorobenzene (3:1) (o-DCB:CB) in a 1:4 (4 mg:16 mg) ratio and stirred for at least 72 h at 80 °C before being used. The photovoltaic devices were fabricated on 25 mm by 15 mm ITO glass substrates with a sheet resistance of ~20 Ω sq^{-1}. The impurities were removed from the ITO glass through a 3-step cleaning process (soap, acetone, isopropanol). The ITO substrates were treated with UV ozone in order to remove the organic molecules and make their surface hydrophilic, before the HTLs film formation. GO thin films (2 nm) were fabricated on mixed cellulose ester membrane with 0.025 µm pores (Millipore) and then transferred onto the ITO substrates. The membranes coated with GO were cut into the substrates size, wetted by immersing them in deionised water and placed the membrane with the film side down onto a substrate surface. The GO film

RSC Advances Accepted Manuscript

This journal is © The Royal Society of Chemistry 20xx

was allowed to dry and adhere to the substrate at room temperature. After 5 h the membrane was removed and the prepared GO films were annealed at 160 °C for 30 minutes. The PEDOT:PSS, purchased from Heraeus, was spin-cast from an aqueous solution on the ITO substrate at 6000 rpm for 60 s and the average thickness of the layer was about 30 nm, followed by baking for 15 min at 120 °C inside a glove box filled with nitrogen. All photoactive layers were subsequently deposited by spin-coating the blend solution at 1000 rpm on top of HTLs until the thickness reached approximately 80 nm, followed by drying it at 60 °C for about 5 min under inert conditions. The TiO_x interlayer was dissolved in methanol (1:200) and then spin-coated on top of the active layer to a thickness of approximately 10 nm (6000 rpm, 40 s) in air.[39]
The samples were heated at 80 °C for 1 min in air. Finally, 100 nm of Al was deposited through a shadow mask by thermal evaporation on the devices. The area of each device is 4 mm^2, as determined by the overlap of ITO and evaporated Al.
The performances of the devices were measured at room temperature with an Air Mass 1.5 Global (A.M. 1.5 G) solar simulator with an intensity of 100 mW cm^{-2}. A reference monocrystaline silicon solar cell from Newport Corp. was used to calibrate the light intensity. The external quantum efficiency measurements were conducted immediately after device fabrication using an integrated system (Enlitech, Taiwan) and a lock-in amplifier with a current preamplifier under short-circuit conditions. The light spectrum was calibrated using a monocrystalline photodetector of known spectral response. The OPV devices were measured using a Xe lamp passing through a monochromator and an optical chopper at low frequencies (~200Hz) in order to maximize the sound/noise ratio. An aperture mask was used to allow the solar light to reach only the active area.

2.2 Space-resolved X-ray characterization

In the present experiment, performed on the beamline ID11 of the ESRF, Grenoble (France), spatially resolved diffraction studies of thin films constituting the active layers of OPV devices were conducted. Due to the constraints imposed by the geometry of the OPV cells (the thickness of each layer was in the range between 50 nm and 200 nm), the use of a strongly focused X-ray beam was required to perform nano-diffraction experiments. In order to preserve the spatial resolution of the nano-focused X-ray beam at approximately 60 nm, the X-ray pathway inside the device was kept as short as possible: to ensure that the X-ray beam probes a small sample width, the OPV devices were cut in a triangular shape and all experiments were conducted with the X-ray beam crossing the tip of the triangle. This procedure provided that the X-ray path across the device was of the order of 100 µm (as evidenced in the SEM image of the sample, shown in figure S1 of the Supplementary Material). Specifically, probing the tip of the triangular shaped sample also avoided an eventual loss of the vertical resolution, should a curvature of the substrate be present. In order to probe each layer comprising the device cross section, the beam direction was set parallel to the cell surface (x-y plane) following the experimental procedure fully described in ref. 51. By progressively shifting the device in the vertical (z) direction, the X-ray beam probed all the layers of the sandwiched specimen, from one electrode to the other.
An X-ray energy of 42 keV was selected using the Laue-Laue monochromator of ID11. The beam was focused horizontally (~5µm size) with a multilayer mirror to increase the photon flux. A vertical line focus (60 nm) was obtained using planar silicon lenses. The X-ray beam was defined by slits located before the lenses and a 1 mm pinhole was mounted between lenses and sample to remove scattering from the slit blades and lenses. Behind the sample, a compound detector system enabled the translation among different detectors. A high-resolution Sensicam X-ray camera (1.3 µm pixel size) was used for alignment purposes. A fibre optic coupled "Frelon" CCD camera detector was used for the diffraction measurements. Once the optimal alignment was reached, the corresponding sample position was set for diffraction by locating the height of the ITO layer in the substrate using the Indium fluorescence signal. X-ray beam size and profile were critical parameters in order to attain the spatial resolution needed for our experiment. The X-ray probe characteristics were obtained using the signal from the ITO thin film. Particularly, the ITO local roughness was determined by AFM measurements to be in the range from 1.0 nm to 2.0 nm (figure S2 of the Supplementary Material), guaranteeing that no significant vertical deflection of the X-ray beam due to the local roughness is expected. The spatial profile of the incident beam was measured by recording the Indium fluorescence as a function of the position of the ITO film with respect to the beam.[51] A beam size of about 60 nm was obtained vertically. This was an outstanding result, the measured beam size being the smallest beam size ever reached on ID11. Following the collection of the diffraction data during repetitive scans a layer-by-layer analysis was performed to extract information on the spatial distribution of the respective XRD peaks.
In addition, by means of a fluorescence detector close to the sample surface, it was possible to perform XRF analysis by tracking the positions of various elements composing the device (In, Sn in the ITO) and thus to identify possible diffusion processes.

2.3 Atomic Force Microscope Characterization

AFM measurements were performed in non-contact mode using a non-commercial air-operating atomic force microscope.[34]

2.3 Energy Dispersive X-Ray Reflectometry (EDXR)

The experimental apparatus used for EDXR[52] consisted of a non-commercial reflectometer featuring a very simple set-up geometry, since neither a monochromator, nor a goniometer are required in the energy dispersive mode, and no movement is needed during the measurements. The Bremsstrahlung of the W anode of an X-ray tube is used as a probe, and a EG&G

RSC Advances Accepted Manuscript

high purity Ge solid-state detector accomplishes the energy scan. EDXR measurements were carried out on the integrated device in its pristine and aged state, corroborating the space resolved XRD analysis of the Al electrode's buried interface.

Results and discussion

Aim of the present study is to provide an accurate space-resolved description of the interface properties and of the active layer polymer component molecular ordering in devices with GO-based HTL compared to those using PEDOT:PSS. The general scheme of the OPV cells used for the experiment is shown in the inset of Figure 1. In such systems the photovoltaic energy conversion rate strongly depends on the nanoscale phase separation during the donor/acceptor heterojunction formation as well as the nano-morphology of the interfaces formed between the active and the charge-collecting layer (Figure 1).

3.1 Photovoltaic Characteristics

Figure 1 displays the illuminated current–voltage (J–V) characteristics of the GO, pr-GO and PEDOT:PSS HTL-based OPV devices. Table 1 reports the averaged photovoltaic characteristics for 10 devices, each consisting of 6 cells: short-circuit current (JSC), fill factor (FF), open circuit voltage (VOC) and Power Conversion Efficiency (PCE). The only difference in the fabrication process between GO and pr-GO devices is that an additional thermal annealing step took place immediately after the spin coating of the GO film.

The results comply with all reported previously and confirm that the pristine GO-based device performance is inferior to that using PEDOT:PSS. Partial reduction of GO is necessary to improve the PCE to the level of devices based on PEDOT:PSS HTL.

In order to understand/interpret the OPV results, an insight into the structural properties characterizing the GO HTL, the photoactive layer as well as the interfaces between different layers is needed.

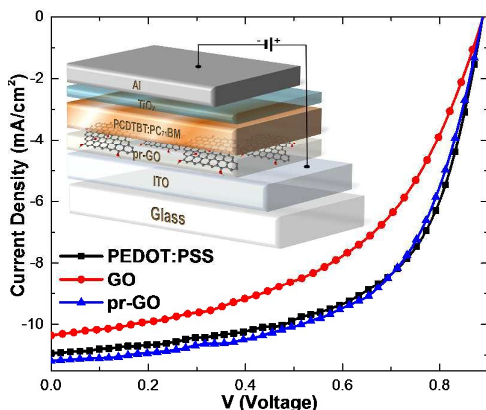

Figure1. 3-D schematic view of the device and comparison of the illuminated current densities for GO, pr-GO HTL-devices and the reference device.

HTL	J_{sc}(A/cm^2)	V_{oc}(V)	FF (%)	PCE (%)
PEDOT:PSS	10.94±0.25	0.89±0.04	60.1±0.3	5.86±0.19
GO	10.35±0.18	0.89±0.05	50.8±0.4	4.69±0.14
pr-GO	11.18±0.27	0.89±0.03	59.8±0.3	5.96±0.20

Table I. Photovoltaic performance comparison of the devices.

3.2 Space-resolved XRD

The integrated OPV devices structure and interface features were probed with a X-ray nano-beam travelling through the cross-sectional areas of the cells. Using this method, we could unveil the structure of each separate layer of the scanned OPV devices. During the measurements, the device was shifted perpendicularly to the X-ray beam, i.e. from the ITO electrode up to the Al cathode and vice versa, while diffraction patterns were continuously recorded. The XRD data (azimuthally averaged) are presented as patterns in a waterfall perspective in Figure 2, in order to better evidence the vertical scan acquisition method.

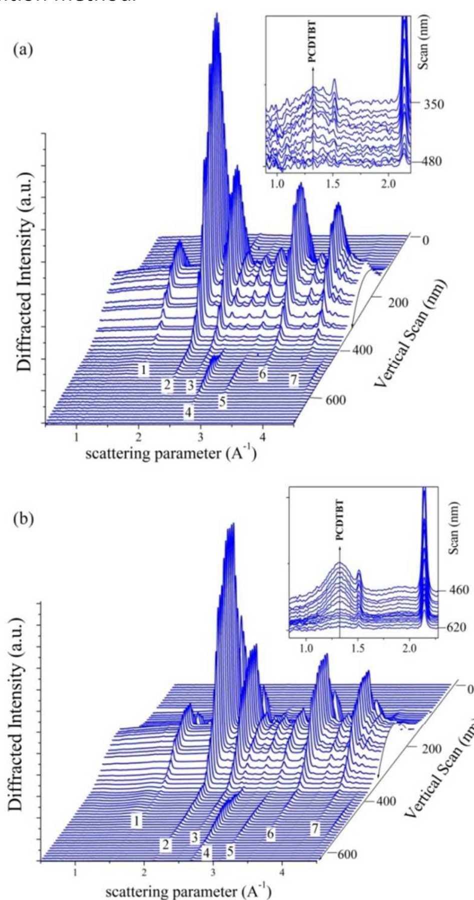

Figure 2. Space-resolved XRD patterns collected on the pristine state of (a) the GO-HTL device and of (b) the reference device. The major peaks are labelled as follows according to JCPDS Nr. 6-41680 for ITO and considering metallic Al with an average unit cell of 4.049 Å: (1) ITO (211) q = 1.521 Å^{-1}; (2) ITO (222) q = 2.146 Å^{-1}; (3) ITO (400) q = 2.475 Å^{-1}; (4) Al (111) q = 2.687 Å^{-1}; (5) Al (200) q = 3.100 Å^{-1}; (6) ITO (440) q = 3.514 Å^{-1}; (7) Al (220) q = 4.380 Å^{-1}; the PCDTBT reflection is highlighted in the inset.

This journal is © The Royal Society of Chemistry 20xx

RSC Advances Accepted Manuscript

Please do not adjust margins

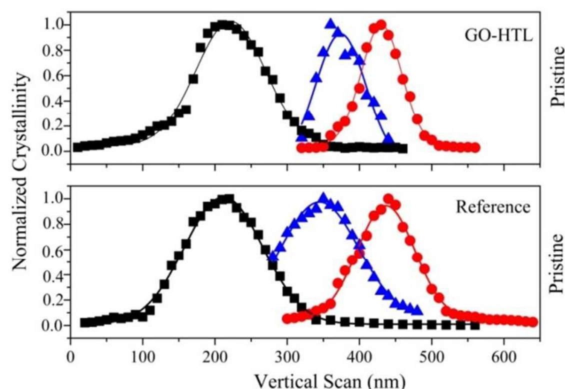

Figure 3. Comparison between the GO-HTL device and the reference device in the pristine state: spatial distribution of the XRD peaks intensities (black squares for ITO, blue triangles for PCDTBT, red circles for Al), as obtained from the analysis of the XRD patterns displayed in Figure 2.

As the beam size was comparable to the thicknesses of the various layers, the scanning procedure allowed discriminating the diffraction signals from each individual layer, providing a cross-sectional stratigraphy of the OPV devices.

Via the layer-wise analysis of these patterns, the spatial distribution of the respective XRD peaks and the description of the molecular ordering of the various layers could be determined (see Figure 3). A systematic analysis of the crystallinity of each reflection (calculated as the normalized area of the peaks via a Gaussian fitting model) was performed and the spatial distribution corresponding to the Al (111), the PCDTBT and the ITO (222) reflections is reported. Indeed these peaks are representative of the distribution of all orientations characterizing the crystallinity of the polycrystalline layers, showing no preferential orientation.

3.2.1. Looking inside the OPV devices. As pointed out above, the spatial resolution attained allowed resolving the contributions corresponding to each layer composing the device. The following can be stated:

Al electrode (red dots): the FWHM of the Gaussian distribution of the Al [111] reflection intensity is (60 ± 10) nm in the case of the GO-HTL device and (80 ± 10) nm for the reference sample. The TiO_x film thickness, as revealed by AFM,[54] is about 10 nm. Such a small amount of material, with thickness in the same range of the X-ray vertical scan sampling steps, was not detected.

Photo-active layer (blue triangles): the space-resolved XRD analysis allowed monitoring the variation of the crystalline contribution of the blend polymer component (the PCDTBT $\pi-\pi$ Bragg reflection, at q = 1.325 $Å^{-1}$).

The data in Figure 3 show that the FWHM of the Gaussian distribution of the intensity of the PCDTBT reflection is (70 ± 10) nm in the case of the GO-HTL device and (110 ± 10) nm for the reference sample. Therefore, the active layer deposition on top of the GO-HTL, under identical conditions, results in a thinner active layer compared to that deposited on PEDOT:PSS. In both cases the polymer component is characterized by a partially crystalline state.

ITO electrode (black squares): the spatial distribution of the XRD intensity of the ITO [222] reflection is practically the same for both the GO-HTL (FWHM = 100 ± 10 nm) and the reference devices (FWHM = 110 ± 10 nm). This is an additional confirmation that the experimental conditions are nearly identical for the systems studied.

However, as shown in Figure 3, the overlapping between the ITO and the active layer signals is much larger in the reference device. In particular, the crossing-over of the ITO and the PCDTB signals occurs when the polymer component is at about 15% of its maximum intensity for the GO-HTL device and at about 50% of that in the reference sample. The percentage of area overlap between the two normalized XRD distributions is about 5 % for the GO-HTL device and about 12 % for the reference sample (both for the ITO and the PCDTBT signlal). This larger leach between the organic layer and the anode can be attributed to the hygroscopic nature of PEDOT:PSS, producing an acid aqueous-environment at the interface that corrodes the ITO electrode. As a consequence, we detect inter-diffusion between the two adjacent layers, in agreement with previous reports on devices using PEDOT:PSS-HTL and based on a P3HT:PCBM active layer.[51,54-56] On the contrary, the GO-HTL device interface is much sharper, and the overlapping between the ITO and the active layer signal is minimal. This is an indication that GO-HTL is able to inhibit the negative effect of diffusion of In ions from ITO into the BHJ.[57]

The above results provide evidence of the different structural and interface characteristics in the pristine state of the GO-HTL device with respect to the reference device.

3.2.2. Tracking inner structural/interface modifications consequent to solar illumination: the protective role of GO-HTL in device aging. A comparative study of the effect of prolonged illumination (24 hours) on the structural/morphological properties of both the GO-HTL and the reference devices was carried out. Results are described in Figure 4 reporting the XRD patterns (in waterfall perspective) collected from the aged GO-HTL device (a) and the aged reference device (b). The results of the analysis of the XRD contributions corresponding to each layer of the OPV cells in both the pristine and aged states for the GO-HTL device and for the reference device are reported in Figure 5. Based on the above data several considerations on device instability can be made.

An encouraging result is that, after aging, the FWHM of the ITO and the BHJ Gaussian distributions are preserved, within the error bars, for both the GO-HTL device and the reference device. Instead, a broader Al distribution was observed in the GO-HTL device after aging. This fact originates from the higher data dispersion next to the device aluminium/air interface and may be imputable to the creation of defects on the cathode free surface, probably due to the sample cutting procedure.

In order to verify this hypothesis EDXR measurements were performed on the pristine and aged state of both the devices, as reported in Figure S3 of the Supplementary Material.

RSC Advances Accepted Manuscript

Please do not adjust margins

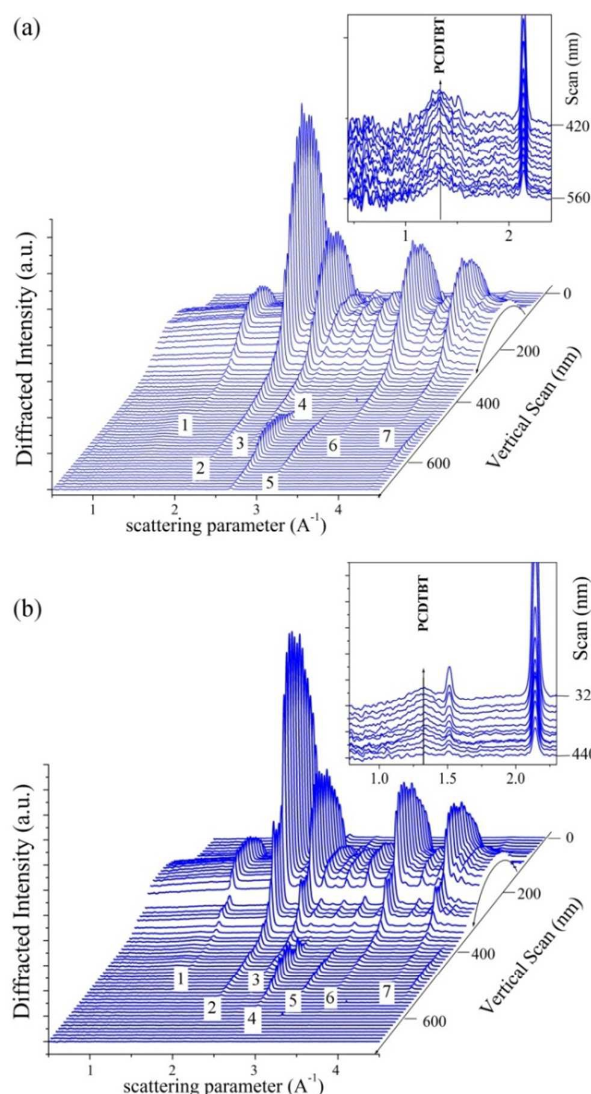

Figure 4. Space-resolved XRD patterns collected, in the aged state, from the GO-HTL device (a) and from the reference device (b). The major peaks are labelled as follows accordingly to JCPDS Nr. 6-41680 for ITO and considering metallic Al with an average unit cell.

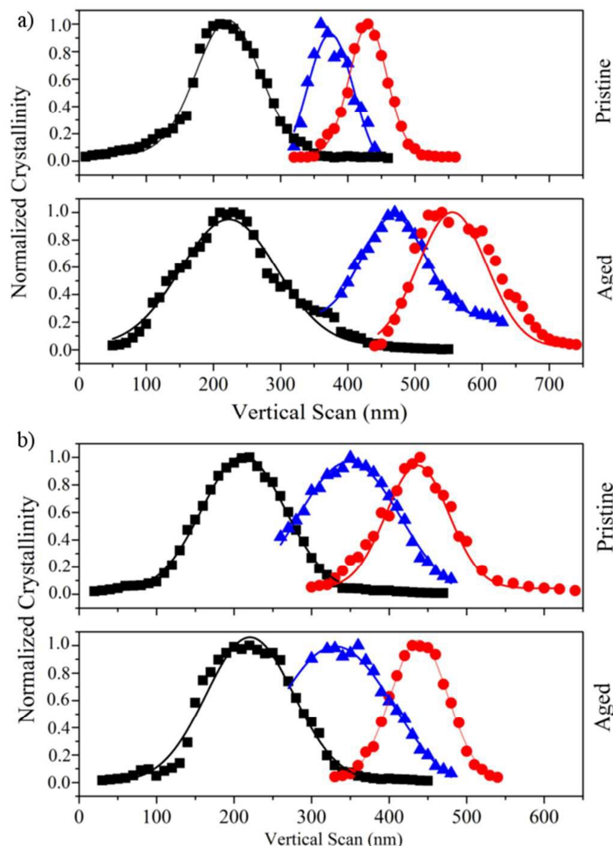

Figure 5. Comparison of the normalized crystallinity of pristine and aged states for the GO-HTL device (a) and for the reference device (b): black squares: ITO, blue triangles: PCDTBT, red circles: Al.

The data show that the average Al film thickness remains unchanged and demonstrate the stability of the electrode's buried interface morphology.

Importantly, such evidence complies with the XRD analysis reported in figure 5: the cross-over between the Al electrode and the polymeric component XRD signals (at about 65% of their intensities) does not change from the pristine to the aged state in neither devices. This fact, underlying the absence of inter-diffusions effects between the two layers, is indication of the protective role of TiO_x ETL in preserving the electrode interface during illumination. Such evidence complies with the above XRD analysis indicating that TiO_x inhibits inter-diffusion at the cathode buried interface.

Finally, the use of GO-HTL is able to limit aging effects at the ITO electrode interface.

Actually, for the reference device the cross-over between the spatial distribution of the XRD intensity pertaining to PCDTBT and the one relative to ITO rises from the initial 50%, in the pristine device state, to about 70% in its aged state (see Figure 5). The leach between the organic layer and the anode quantified considering that the percentage of area overlap between the two normalized XRD distributions increased by 6% after aging (area overlapp rising from about 12 % to approximately 18 % for both ITO and PCDTBT). This analysis is consistent with additional In diffusion occurring at the ITO interface in contact with the blend as a consequence of aging, as previously suggested.[58]

At the same time, in the aged state of the device, a modification of the XRD signal related to the polymeric component is detected in the patterns corresponding to the interfacial region of the blend in contact with the ITO/PEDOT:PSS interface: the PCDTBT reflection gets broader and an overall loss in intensity is found (it was not possible to obtain a suitable fit and the corresponding points in Figure 5 are missing). There is therefore strong indication that, at the blend buried interface, the polymer component includes crystallites of smaller size and is characterized by a greater

 This journal is © The Royal Society of Chemistry 20xx

RSC Advances Accepted Manuscript

Please do not adjust margins

amorphous contribution. This evidence is consistent with the clear further diffusion of In at the blend buried interface, which is promoted by illumination.[58] This mechanism perturbs the PCDTBT crystallinity distribution. A further confirmation that In diffusion occurs at the ITO/PEDOT:PSS interface (within about 15nm) was catered by space-resolved XRF (performed simultaneously to XRD) tracking the In signal profile through the device depth (see Figure S4 of the Supplementary Material). This result is in agreement with what observed at the ITO/PEDOT:PSS interface for a similar OPV device (using PEDOT:PSS as HTL and P3HT:PCBM as BHJ):[47] the XRF analysis uncovered the diffusion of In from the ITO substrate into the adjacent PEDOT:PSS layer.

In contrast to that, the data of Figure 5(a) suggest that in the case of the GO-HTL aged device there is no inter-diffusion between the blend and ITO: the cross-over between the ITO and the BHJ signals is not affected by the aging of the cell. This denotes that the use of GO as HTL gives rise to an enhanced stability of the BHJ buried interface.

Conversely, the interface between the blend and ITO becomes much sharper: the relative distance between the centroids of the ITO and PCDTBT distributions is increased by about 100 nm. This is a significant effect and a possible explanation is that illumination triggers a morphological modification occurring at the interfacial region between ITO and the blend, i.e. involving the GO-HTL.

Such protective role of GO-HTL inhibiting inter-diffusion is also witnessed by the XRF results (Figure 6).EDXR measurements on the pristine and aged state of the reference device (figure S3 of the Supplementary Material) confirm the results of the above analysis: the amplitude of the fringes corresponding to the PEDOT:PSS film is largely reduced after aging, indicating that its buried interface to ITO becomes less sharp (the interface roughness increases): a further hint of In diffusion inside the HTL. Figure 6A and Figure 6B show the XRF spatial mapping for the pristine and aged state, respectively, of the device. The XRF data, analysed using the PyMca program developed at the ESRF,[59] provided the spatial evolution of the Indium fluorescence line intensity presented in Figure 6C.

It is evident that the two profiles, relative to the device in the pristine state and in the aged state, are perfectly overlapping. Such outcome is consistent with the above analysis implying that, GO-HTL blocked In diffusion within the inner part of the device.

This aspect is an important pathway of device aging, since In diffuses throughout all layers in the device and ends up on the outer surface of the Al electrode.

In order to fully describe the observed morphological changes induced at the PCDTBT/GO-HTL interface upon aging, AFM measurements were performed on the glass/ITO/GO substrate.

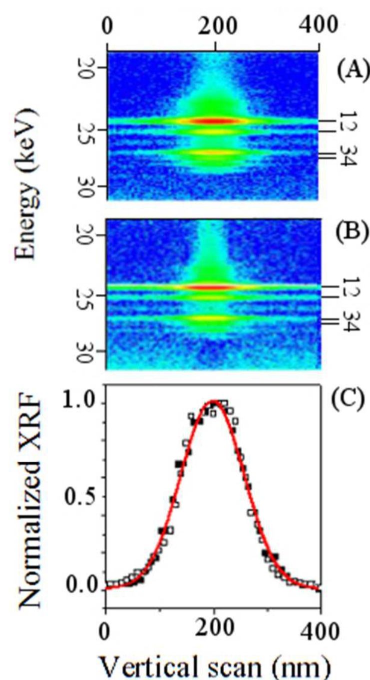

Figure 6. XRF partial mapping of the pristine (A) and aged (B) state of the GO-HTL device. The labelled fluorescence lines are: $InK_{\alpha1,2}$ (1); $SnK_{\alpha1,2}$ (2) $InK_{\beta1}$ (3); and $SnK_{\beta1}$(4). (C) Corresponding spatial distributions of the Indium fluorescence line intensity: device in the pristine state [empty squares] and in the aged state [black squares].

The data comparing the GO and the pr-GO sample surface before and after illumination, performed in the same conditions as the devices under study, are reported in Figure 7. A remarkable modification of the GO surface is observed for the GO sample. The AFM analysis (Figure 7a), showed that illumination produced an enormous increase in the GO surface roughness (rms = 2 nm for pristine state vs. rms = 70 nm for aged state). It clearly appears that GO acts as a sponge, absorbing the H_2O molecules present in the atmosphere. Hence, a possible explanation of the observed roughness increase in GO in the aged state is that the release of water molecules from the interlayer surface may reshuffle the deposited layers.

In the case of the pr-GO (annealed at 160 °C), the sample morphology (reported in Figure 7b) looks almost the same before and after illumination. No appreciable modification can be identified as a consequence of light aging, confirming the superior stability of the pr-GO film, which in fact is demonstrated in the photovoltaic performance (see section 3.4 below).

FTIR analysis comparing the pristine and illuminated state of the glass/ITO/GO sample (Figure S5 in the Supplementary Material) confirmed the above hypothesis on the origin of such morphological modification. In the pristine state, the spectral markers of the hygroscopic nature of GO are present.[60,61] In the aged state no spectral markers of free water are present, indicating loss of H_2O.

RSC Advances Accepted Manuscript

Please do not adjust margins

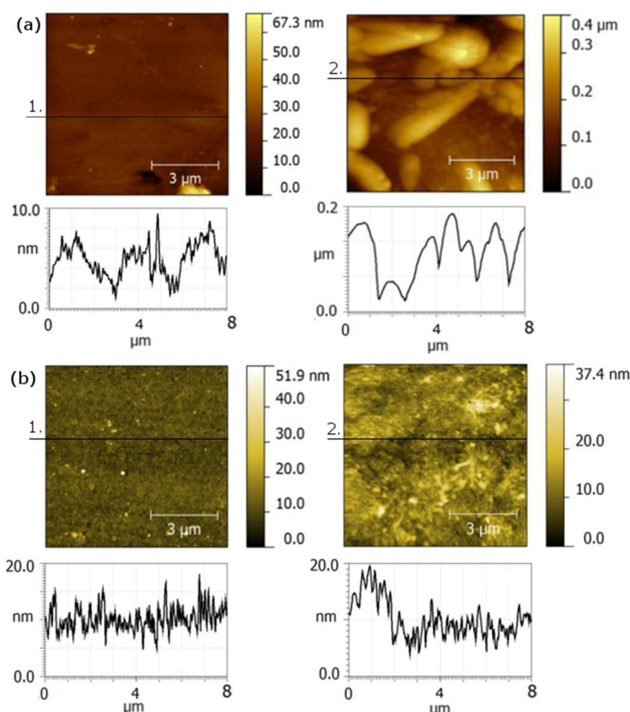

Figure 7. AFM images featuring line profiles: **(a)** GO-HTL in the pristine (left) and aged (right) state. The following roughness values were deduced: pristine state (left) rms = 3.6 nm; aged state (right) rms = 60 nm. **(b)** pr-GO-HTL (160°C annealed film): in the pristine (left) and aged (right) state. The following roughness values were deduced: pristine state rms = 3.8 nm (left); aged state (right) rms = 3.9 nm.

FTIR analysis suggests also a partial reduction of GO as a consequence of solar illumination: an effect that confirms that a photoreduction process takes places during solar illumination, as in the case of laser induced reduction of the GO. This inference is supported by a former work, in which a graphite film is effectively exfoliated into graphene by focused solar irradiation.[62]

The origin of morphological modifications of GO in Figure 7a appears to be associated to a partial thermal and non-thermal photochemical reduction of GO,[48] due to the high temperature reached upon solar irradiation, removing the trapped water molecules between the layers of GO.

We have thus directly substantiated why the pr-GO-based devices are superior to the pristine GO devices. The thermal annealing process at 160°C removes actually the water molecules trapped between the layers of GO. The stability of the surface topography of the pr-GO film is clearly demonstrated in Figure 7b, indicating that solar illumination does not have an effect on the pr-GO, differently from the case of GO, since a partial reduction already has occurred as a result of thermal annealing, inhibiting the penetration of water molecules into the photoactive layer.

3.4 Structure-properties correlation: PV aging

This investigation has produced evidence that a partial reduction of GO, as obtained by thermal annealing, could potentially stabilize the BHJ buried interface. This is an important finding, since the annealing procedure is usually not applied to devices exhibiting PCDTBT as donor polymer, as opposed to other polymer systems.

In our earlier work, the use of spin-coated GO HTL in OPVs based on P3HT:PCBM BHJ was reviewed.[37] In the case of P3HT as a donor material, the optimized devices required post-fabrication annealing at 160°C to increase the crystallinity of the polymer and hence the charge transport. This thermal treatment affects not only the blend morphology, but also leads to the partial reduction of the GO thin film. In contrast to P3HT, the post-fabrication annealing in BHJs, based on PCDTBT, has the opposite result. It affects negatively the polymer structure by disrupting the PCDTBT molecules π-π stacking and deteriorates in this way the device performance.[63,64] In this case, the partial reduction of the GO coated ITO substrate should be activated by thermal annealing at 160°C before the active layer deposition to set off the effective removal of the water molecules trapped between the layers of GO. This argument was underpinned by a systematic study of the influence of the annealing temperature of GO on the photovoltaic properties, in which all the GO devices annealed at temperatures less than 150°C, did not show a PCE comparable with that of PEDOT:PSS. A behaviour which is explained by taking into account that the temperature threshold for thermal reduction of GO in air is 150°C.[65]

By comparing the stability of the pristine GO based devices to the thermally treated (pr-GO) ones, we found that the latter scored better in terms of both PCE and lifetime. The pr-GO is hydrophobic and can potentially act as an oxygen/moisture barrier impeding the oxygen/water diffusion into the photoactive layer. The barrier characteristics may be also attributed to the closely packed hexagonal atomic structure of graphene, which is shown to prevent even the permeation of hydrogen.[66] This is a feature which is not present in the GO film, in which the GO sheets are randomly oriented and widely spaced,[67] creating permeation paths. In a recent study, it was shown that the annealing of the GO to pr-GO induces a restoration of the pristine graphene nano-islands, which in fact causes the clogging of permeation paths, and leads to greater diffusion lengths and thus to longer degradation time.[68]

The effect of GO partial reduction on the OPV device's stability was examined: OPV devices were tested in open circuit mode with continuous solar illumination (100 mW/cm2) and without encapsulation, in order to allow humidity to directly affect their performance. As shown in Figure 8 a, the aging in PEDOT:PSS/PCDTBT:$PC_{71}BM$ device after 20 h of continuous solar illumination was detected to be approximately 45% of the initial PCE. Differently from that, in pr-GO/PCDTBT:$PC_{71}BM$ devices, the degradation rate on the same time scale is much slower, as approximately 65% of its initial PCE is preserved. In GO HTL-based devices the degradation process reached almost saturation after 45 hours of solar illumination, while the PEDOT:PSS HTL devices exhibited an approximately linear PCE decay. This result clearly demonstrates the pr-GO role as a protecting layer against humidity and In diffusion into the

RSC Advances Accepted Manuscript

This journal is © The Royal Society of Chemistry 20xx

Journal Name

ARTICLE

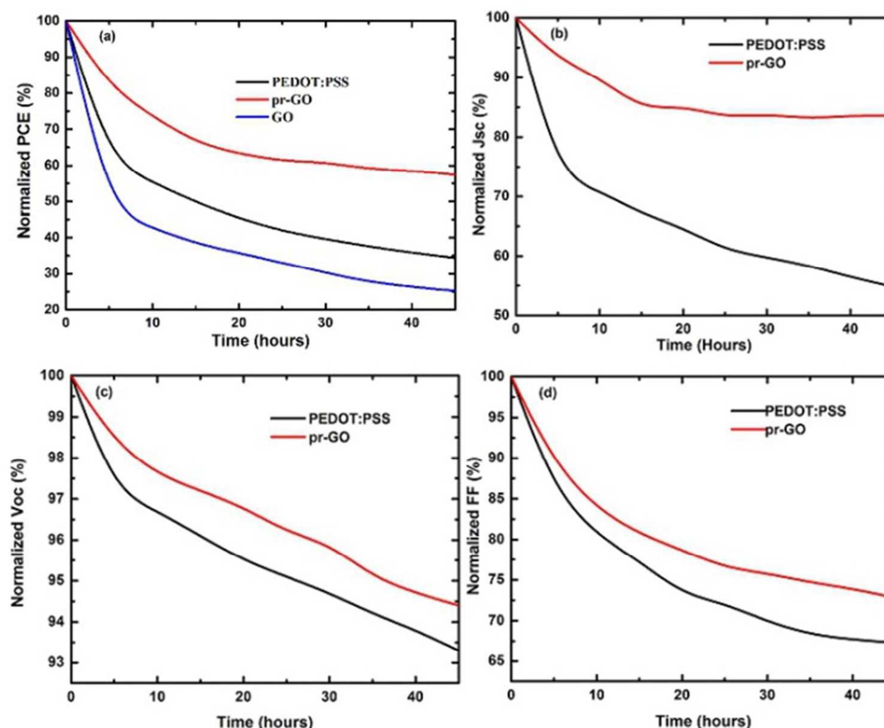

Figure 8. PCE, Jsc, Voc and FF changes of OPVs based on PEDOT:PSS and pr-GO, respectively, under prolonged solar irradiation.

photoactive layer which is in full agreement with the results described above.

In addition, the better passivation ability of partially reduced GO against moisture and oxygen as compared to the conventional PEDOT:PSS endorses the adoption of pr-GO as HTL for achieving long-term stable OPVs.[69]

On the other hand, the as deposited GO demonstrates lower device stability compared to thermally reduced GO-based devices, mainly due to residual oxygen and water molecules in GO, because reduction of oxygen-containing groups and removal of the residual solvent between the layers of GO during solar illumination occur simultaneously.

Exploring the PV parameters in order to understand the different behaviour of the HTL materials Figure 8 b,c,d shows the evolution of the respective PV parameters versus exposure time for both tested devices. For each data point of the aging curves, a complete J–V characteristic was recorded and the normalized Jsc, FF, Voc and PCE values were subsequently calculated. It can be easily understood that there is a significant enhancement in pr-GO-based device durability, mainly due to the protective function of pr-GO against humidity and In diffusion into the photoactive layer. The main difference is detected in Figure 8b (Jsc), where the decay rate of PEDOT:PSS based devices is much faster. In particular, after 40 hours of continuous illumination the PEDOT:PSS based device retains ~55% of its initial Jsc compared to pr-GO based device which retains ~82% of its initial Jsc in the same time scale. Such photocurrent loss (in PEDOT:PSS case) can be attributed to morphological instabilities that cause In diffusion inside the active layer.

To further support the results obtained from the I-V curves before and after solar illumination the incident photon-to electron conversion efficiency (IPCE) curve of the devices were measured and compared (Figure S6 a,c,e in the Supplementary Material). Both before and after illumination pr-GO based OPV devices exhibit the highest external quantum efficiency (EQE) values and the Jsc obtained from the integration of the IPCE spectra is in agreement with the actual measured JSC values (1.5% difference). After 20 and 40 hours of solar illumination both PEDOT:PSS and GO-based devices exhibit a significant EQE values decay, with the latter presenting the highest decrease. In addition, the absorbance spectra (Figure S6 b,d,f in the Supplementary Material) of the three different HTL-based devices were measured at three different time points

RSC Advances Accepted Manuscript

under prolonged solar illumination (0h, 20h and 40h). It is clear that the slight reduction of GO under solar illumination affects the active layer morphology and thus its absorbance ability (Figure S6 b,d,f in the Supplementary Material). The higher stability of the pr-GO-based devices stems from its nearly neutral properties with few surface oxygen functionalities and its inherent passivation ability against oxygen and moisture.[68] Furthermore, the lower device stability of PEDOT:PSS-based device compared to pr-GO-based one, is due to the fact that PEDOT:PSS is spin coated from highly acidic suspension (pH~1), which erodes ITO electrode and causes In diffusion into the photoactive layer, negatively affecting its morphology. Also, water molecules can readily penetrate into the hygroscopic PEDOT:PSS layer, resulting in degraded device performance. The results further support that in pr-GO-based device the morphological modifications after solar illumination are minimum, while in the case of GO and PEDOT:PSS HTLs, the active layer morphology is strongly affected.

Conclusions

In summary, the present high spatial resolution combined XRD/XRF study of integrated OPV devices has made it possible to reveal the detailed structure of the different cell layers and determine the aging effects induced upon prolonged solar irradiation and consequent thermal reduction. In particular, data from the reference device elucidate the occurrence of an interface aging effect of the blend at the HTL-ITO electrode side. Reversely, the use of pr-GO-HTL stabilizes the BHJ buried interface. The present analysis shows that replacing PEDOT:PSS with pr-GO as HTL allows enhancing the active layer buried interface properties. The positive impact of the inhibition of the BHJ buried interface degradation pathway on the stability of the PV parameters are discussed on the basis of aging curves collected from the same devices, also evidencing the positive effect of performing a partial reduction of the GO HTL by thermal annealing prior to BHJ deposition.

Space-resolved X-ray techniques complemented by EDXR measurements, allowed detecting the aging effects, which limit the performance of OPV cells and disclose a new/possible roadmap toward an optimum strategy for enhancing the stability of these devices. The use of TiO_x as ETL is shown to create a protective barrier action against aging effects at the aluminium electrode's buried interface for both reference and GO HTL systems.

Importantly, the use of GO as HTL inhibits the severe aging of the BHJ interface with HTL-ITO, which was conversely observed for the reference device.

As an outcome, employing pr-GO HTLs appears to be an important step towards the development of novel architectures underlying more stable organic devices.

Besides the far-reaching impact due to the elucidation of the decisive role of pr-GO HTL in protecting OPV devices from degradation, this work paves the way for the future development of high spatial resolution in-situ diagnostics for nanolayered structures.

Acknowledgements

These research activities have received funding from the European Union Seventh Framework Programme under grant agreement n°604391 Graphene Flagship. The authors are grateful for the support of the COST Action HINT (MP1202). They are greatly indebted to Prof L. Vincze for invaluable discussions and to Mr. M. Guaragno for his technical support in performing the FTIR measurements.

Notes and references

1 G. Li, R. Zhu, Y. Yang, *Nat. Photonics,* 2012, **6**, 153.
2 N. S. Sariciftci, L. Smilowitz, A. J. Heeger, F. Wudl, *Science* 1992, **258**, 1474.
3 G. Yu, J. Ga, J. C. Hummelen, F. Wudl, A. J. Heeger, *Science* 1995, **270**, 1789.
4 J. B. You, L. T. Dou, K. Yoshimura, T. Kato, K. Ohya, T. Moriarty, K. Emery, C. C. Chen, J. Gao, G. Li, Y. Yang, *Nat. Commun.*, 2013, **4**, 1446.
5 C.-C. Chen, W.-H. Chang, K. Yoshimura, K. Ohya, J. You, J. Gao, Z. Hong and Y. Yang, *Advanced Materials,* 2014, **26**, 5670.
6 R. Steim, F. R. Koglera, C. J. Brabec, *J. Mater. Chem.*, 2010, **20**, 2499.
7 J. Y. Kim, S. H. Kim, H. H. Lee, K. Lee, W. Ma, X. Gong, A. J. Heeger, *Adv. Mater*., 2006, **18**, 572.
8 C. J. Brabec, V. Dyakonov, U. Scherf, Organic Photovoltaics: Materials, Device Physics and Manufacturing Technologies, Wiley-VCH, Weinheim 2008.
9 F. Zhang, M. Ceder, O. Inganas, *Adv. Mater.*, 2007, **19**, 1835.
10 H. Yan, P. Lee, N. R. Armstrong, A. Graham, G. A. Evmenenko, P. Dutta, T. J. Marks, *J. Am. Chem. Soc.*, 2005, **127**, 3172.
11 M. Jorgensen, K. Norrman, F. C. Krebs, *Sol. Energy Mater. Sol. Cells*, 2008, **92**, 686.
12 G. Kakavelakis, D. Konios, E. Stratakis, E. Kymakis, *Chem. Mater.*, 2014, **26**, 5988.
13 G. Viskadouros, D. Konios, E. Kymakis, E. Stratakis, *App.Phys. Lett.,* 2014, **105**, 203104.
14 M. M. Stylianakis, M. Sygletou, K. Savva, G. Kakavelakis, E. Kymakis, E. Stratakis, *Adv. Opt.l Mater. ,* 2015, DOI: 10.1002/adom.201400450.
15 D. Konios, C. Petridis, G. Kakavelakis, M. Sygletou, K. Savva, E. Stratakis, E. Kymakis, *Adv. Funct. Mater.,* 2015, **25**, 2206.
16 S. S. Li, K. H. Tu, C. C. Lin, C. W. Chen, M. Chhowalla, *ACS Nano*, 2010, **4**, 3169.
17 I. P. Murray, S. J. Lou, L. J. Cote, S. Loser, G. J. Kadleck, T. Xu, J. M Szarko, B. S. Rolczynski, J. E Johns, J. Huang, L. Yu, L. X. Chen, T. J. Marks, M. C. Hersam, *J. Phys. Chem. Lett.*, 2011, **2**, 3006.
18 K. P. Loh, Q. Bao, G. Eda, M. Chhowalla, *Nat. Chem.*, 2010, **2**, 1015.
19 E. Stratakis, K. Savva, D. Konios, C. Petridis, E. Kymakis, *Nanoscale*, 2014, **6**, 6925.
20 D. Konios, M. M. Stylianakis, E. Stratakis, E. Kymakis, *J. Colloid And Interface Science*, 2014, **430**, 108-112.
21 F. Bonaccorso, Z Sun, T Hasan, AC Ferrari, *Nat. Photonics* 2010, **4** , 611
22 J. Liu, M. Durstock, L. Dai., *Energy Environ. Sci*., 2014, **7**, 1297
23 B. Paci, A. Generosi, V. Rossi Albertini, P. Perfetti, R. De Bettignies, M. Firon, J. Leroy, C. Sentein, *Appl. Phys. Lett.*, 2006, **89**, 043507.
24 B. Paci, A. Generosi, V. Rossi Albertini, R. De Bettignies, C. Sentein, *Chem. Phys. Lett.*, 2008, **461**, 77.

RSC Advances Accepted Manuscript

25 B. Paci, A. Generosi, V. Rossi Albertini, P. Perfetti, R. De Bettignies, C. Sentein, *Sol. Energy Materials and Solar Cells*, 2008, **92**, 799.
26 B. Paci, A. Generosi, V. Rossi Albertini, P. Perfetti, R. De Bettignies, M. Firon, J. Leroy, C. Sentein, *Appl. Phys. Lett.*, 2005. **87**, 194110.
27 A. W. Hains, T. J. Marks, *Appl. Phys. Lett.*, 2008, **92**, 1.
28 M. Kemerink, S. Timpanaro, M. M. de Kok, E. A. Meulenkamp, F. J. Touwslager, *J. Phys. Chem. B*, 2004, **108**, 18820.
29 A. Garcia, G. C. Welch, E. L. Ratcliff, D. S. Ginley, G. C. Bazan, D. C. Olson, *Adv. Mater.*, 2012, **24**, 5368.
30 M. S. White, D. C. Olson, S. E. Shaheen, N. Kopidakis, D. S. Ginley, *Appl. Phys. Lett.*, 2006, **89**, 143517.
31 R. Po, C. Carbonera, A. Bernardi and N. Camaioni, *Energy Environ. Sci.*, 2011, **4**, 285.
32 M. T. Greiner, M. G. Helander, W. M. Tang, Z. B. Wang, J. Qiu, Z. H. Lu, *Nat. Mater.*, 2012, **11**, 76.
33 B. Paci, G. D. Spyropoulos, A. Generosi, D. Bailo, V. Rossi Albertini, E. Stratakis, E. Kymakis, *Adv. Funct. Mater.*, 2011, **21**, 3578.
34 B. Paci, A. Generosi, V. Rossi Albertini, R. Generosi, P. Perfetti, R. De Bettignies, C. Sentein, J. *Physical Chemistry C*, 2008, **112**, 9931.
35 B. Paci, A. Generosi, D. Bailo, V. Rossi Albertini, R. De Bettignies, *Chem. Phys. Lett.*, 2010, **494**, 69.
36 B. Paci, A. Generosi, V. Rossi Albertini, R. De Bettignies, *J. Phys. Chem. C*, 2009, **113**, 19740.
37 D. Chirvase, J. Parisi, J. C. Hummelen, V. Dyakonov, *Nanotechnology*, 2004, **15**, 1317.
38 E. Stratakis, M. Stylianakis, E. Koudoumas, E. Kymakis, *Nanoscale,* 2013, **5**, 4144
39 S.S. Li , K.H. Tu , C.C. Lin ,C.W. Chen , M. Chhowalla, *ACS Nano*, 2010, **4** , 3169.
40 J. Liu, Y. Xue, L. Dai, *J. Phys. Chem. Lett.*, 2012, **3**, 1928.
41 C. T. G. Smith, R. W. Rhodes, M. J. Beliatis, K. D. G. I. Jayawardena, L. J. Rozanski, C.A. Mills, and S.R.P. Silva, *Appl. Phys. Lett.,* 2014, **105**, 073304.
42 X. D. Liu, H. Kim and L. J. Guo,*Org. Electron*., 2013,**14**, 591.
43 S.-H. Kim, C.-H. Lee, J.-M. Yun, Y.-J. Noh, S.-S. Kim, S Lee, S. M. Jo, H.-I. Joh, S.-I. Na, *Nanoscale*, 2014, **6**, 7183.
44 D. Yang , L. Zhou , W. Yu, J. Zhang ,C. Li, *Adv. Energy Mater.,* 2014, **4**, 1400591.
45 J. S. Yeo, J. M. Yun, Y. S. Jung, D. Y. Kim, Y. J. Noh, S. S. Kim, S. I. Na, *J. Mater. Chem. A*, 2014, **2**, 292.
46 E. Kymakis, K. Savva, M.M. Stylianakis, C. Fotakis, E. Stratakis, *Adv. Funct. Mater.*, 2013, **23**, 2742.
47 L. J. Cote, R. Cruz-Silva, J. Huang, *J. Am. Chem. Soc*., 2009, **131**, 11027.
48 Y.-L. Hang, L. Guo, H. Xia, Q.-D. Chen, J. Feng, H.-B. Sun, *Adv. Opt. Mater.* 2014, **2**, 10.
49 H. L. Poh, F. Sanek, A. Ambrosi, G. Zhao, Z. Sofer, M. Pumera, *Nanoscale*, 2012, **4**, 3515.
50 Z. He, C. Zhong, X. Huang, W.-Y. Wong, H. Wu, L. Chen, S. Su, Y. Cao, *Adv. Mater.*, 2011, **23**, 4636.
51 B. Paci, D. Bailo, V. Rossi Albertini, J.Wright, C. Ferrero, G.D. Spyropoulos, E. Stratakis, E. Kymakis, *Adv. Mater*., 2013, **25**, 4760.
52 V. R. Albertini, B. Paci, A. Generosi, *J. Phys. D.* 2006, **39**, 461.
53 G. Kakavelakis, E. Stratakis, E. Kymakis E., *Chem. Comm.,* 2014, **50**, 5285.
54 D.-W. Wang, K.-H. Wu , I.R. Gentle, G.Q. Lu, *Carbon*, 2012, **50**, 333.
55 X. Wang, X. Li, L. Zhang, Y. Yoon, P.K. Weber, H. Wang, J. Guo, H. Dai, *Science*, 2009, **324**, 768.
56 J. L. Bahr, J. P. Yang, D. V. Kosynkin, M. J. Bronikowski, R. E. Smalley, J.M. Tour, *J. Am. Chem. Soc.*, 2001, **123**, 6536.
57 Ming-Chung Chen, Yi-Shiang Chiou, Jian-Ming Chiu, Abebe Tedla and Yian Tai, *J. Mater. Chem. A*, 2013, **1**, 3680.
58 F. C. Krebs, K. Norrman, *Prog. Photovol. Res. Appl.,* 2007,**15**, 697.
59 V. A. Solé, E. Papillon, M. Cotte, Ph. Walter, J. Susini, *Spectrochim. Acta B,* 2007, **62**, 63.
60 W. Chen, L. Yan, *Nanoscale*, 2010, **2**, 559.
61 B. C. Smith, Fundamentals of Fourier Transform Infrared Spectroscopy, CRC Press, Taylor & Francis Group, Second Edition 2011.
62 V. Eswaraiah, S. S.J. Aravind, S. Ramaprabhu, *J. Mater. Chem.,* 2011, **21**, 6800
63 T. Wang, A. J. Pearson, A. D. F. Dunbar, P. A. Staniec, D. C. Watters, H. Yi, A. J. Ryan, R. A. L. Jones, A. Iraqi, D. G. Lidzey, *Adv. Funct. Mater.*, 2012, **22**, 1399.
64 O. Synooka, K. R. Eberhardt, C. R. Singh, F. Hermann, G. Ecke, B. Ecker, E. von Hauff, G. Gobsch, H. Hoppe, *Adv. Energy Mater.*, 2014, **4**, 1300981.
65 W. Chen, L. Yan, *Nanoscale*, 2010, **2**, 559.
66 O. Leenaerts , B. Partoens , F. M. Peeters , *Appl. Phys. Lett.* **2008** , *93* , 193105.
67 D. Li, M. Muller, S. Gilje, R. B. Kaner and G. G. Wallace*, Nat. Nanotechnol.,* 2008, **3**, 101.
68 H. Yamaguchi, J. Granstrom, W. Nie, H. Sojoudi, T. Fujita, D. Voiry, M. Chen, G. Gupta, A. D. Mohite, S. Graham, M. Chhowalla, *Adv. Energy Mater.*, 2014, **4**, 1300986.
69 Z. Liu, J. Li, F. Yan, *Adv. Mater.*, 2013, **25**, 4296.

RSC Advances Accepted Manuscript

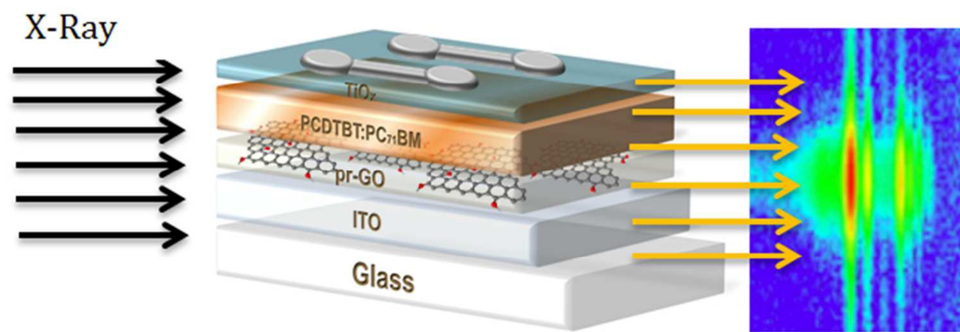

234x81mm (72 x 72 DPI)

RSC Advances Accepted Manuscript